Compact and versatile neutron imaging detector with sub-4μm spatial resolution based on a single-crystal thin-film scintillator

ALESSANDRO TENGATTINI,[1,2,*] NIKOLAY KARDJILOV,[3] LUKAS HELFEN,[2] PAUL-ANTOINE DOUISSARD,[4] NICOLAS LENOIR,[1] HENNING MARKÖTTER,[5] ANDRÈ HILGER,[3] TOBIAS ARLT,[3] MELANIE PAULISCH,[3] THOMAS TUREK,[6] AND INGO MANKE[3]

[1]*Université Grenoble Alpes, CNRS, Grenoble INP, 3SR, 38000 Grenoble, France*
[2]*Institut Laue-Langevin, 71 Avenue des Martyrs, Grenoble 38000, France*
[3]*Institute of Applied Materials, Helmholtz-Zentrum Berlin for Materials and Energy, Hahn-Meitner-Platz 1, 14109 Berlin, Germany*
[4]*ESRF - The European Synchrotron, 71 avenue des Martyrs 38000 Grenoble, France*
[5]*Bundesanstalt für Materialforschung und -Prüfung (BAM), Unter den Eichen 87, 12205 Berlin, Germany*
[6]*Institute of Chemical and Electrochemical Process Engineering, Clausthal University of Technology, Clausthal-Zellerfeld, Germany*
[*]*tengattini@ill.fr*

Abstract: A large and increasing number of scientific domains pushes for high neutron imaging resolution achieved in reasonable times. Here we present the principle, design and performance of a detector based on infinity corrected optics combined with a crystalline $Gd_3Ga_5O_{12} : Eu$ scintillator, which provides an isotropic sub-4 μm true resolution. The exposure times are only of a few minutes per image. This is made possible also by the uniquely intense cold neutron flux available at the imaging beamline NeXT-Grenoble. These *comparatively* rapid acquisitions are compatible with multiple high quality tomographic acquisitions, opening new venues for *in-operando* testing, as briefly exemplified here.

1. Introduction

High resolution imaging is an essential probing tool for solving a number of open scientific questions. In x-ray imaging, resolutions below 10 μm are commonplace in laboratory scanners, with advanced commercial machines even achieving sub-micron resolutions. In neutron imaging, sub-10 μm resolutions are comparatively harder to achieve, also due to difficulties in the detection of neutral particles, as well as because of the typically limited neutron flux (here addressed by the high flux available at the Institut Laue Langevin). However, to solve many scientific and engineering problems, we still need to rely on the unique properties of neutrons, (*e.g.*, isotope sensitivity, high attenuation to some light elements, low attenuation to some heavy elements), as detailed in several comprehensive reviews [1–5].

These open questions range from the water distribution in automotive membrane electrode assembly (MEA) of operating fuel cells to the development of dendrites in lithium batteries, and from the role of water in the hydraulic fracturing of rocks or membrane structures to the hydrogen diffusion in metals, to only mention a few. With such high demand, it is unsurprising that a number of approaches have been proposed across the years for acquiring high resolution neutron images.

But independent of the actual detection resolution, a magnification in the neutron imaging process (*e.g.*, through a magnified projection approach or an imaging-lens based approach) directly allows for obtaining an increased spatial resolution.

This has been successfully demonstrated for example by the use of axisymmetric focussing mirrors (Wolter optics) [6], which are being perfected at NASA and NIST.

A reflective grazing-angle imaging lens (similar to x-ray telescopes) allows for taking advantage of a higher divergence (compared to the classical pinhole collimation approach) of the incident beam and forms a magnified image of the specimen after the lens. The current prototypes are mainly limited by aberrations and achieve a maximum resolution of a few tens of microns, although promising upgrades are foreseen in the future.

On the other hand the development of new detector systems helps to increase their intrinsic resolution. For example, approaches based on single event reconstruction provide increased spatial resolution (as low as $2\,\mu m$, [7]), albeit they come at the cost of the acquisition of about 10^5 frames per radiography. With the current technology this translates to more than one hour per radiograph and does not account for the time needed for the data treatment (*e.g.*, centroid recuperation). In very recent works [8] the potential of this approach is further developed for Time of Flight imaging. Particular attention is therein given to the analysis of the photon imaging detection procedure (the identification of photons by grouping pixels corresponding to one photon) as well as the neutron imaging procedure, which identifies neutrons by grouping photons.

In some special conditions (*e.g.*, for the study of fuel cells) a tilting of "standard" detector setup can be adopted to increase anisotropically the resolution, even to the sub-10 μm range *e.g.*, [9].

Concerning neutron detection resolution, it is well known that in neutron-sensitive microchannel plate (MCP) detectors, the maximum spatial resolution is of about 15 μm [10–12], as currently limited by the diameter of the micropores, the bias angle as well as the range of the charged particle (while still allowing for very high temporal resolution of 750 ps, ideal for pulsed imaging).

LiF crystals are used as a detection system by studying their color center formation ([13–15]). While this method allows one to acquire radiographs with resolutions as low as 5.4 μm, it requires a long exposure for each radiograph followed by the analysis of the lithium plate by fluorescent microscopes, rendering tomography unpractical.

A Timepix-based detector coated with a ~1;μm thick layer of LiF or B4C can also be used in order to track ion particle paths ([16,17]). This yields a sub-pixel resolution down to few tens of microns over a large area of a few tens of square cm, albeit the very thin coating limits the fraction of captured flux.

The most common approach to high-resolution neutron detection lies in the concept of the indirect detection scheme: neutrons are being captured by a neutron-absorbing material and its scintillation characteristics are used to emit visible light which is being magnified onto a 2D light-sensitive imaging sensor, *e.g.*, based on CCD or CMOS technologies. To couple the visible light between the two, optical systems composed of one or more magnifying lenses are generally employed, whether commercially available, or tailored to a specific setup. Fiber optics also have been successfully employed to reduce the broadening of light solid angle and enhance magnification [18,19] down to a resolution of 15 μm. The main shortcoming of fiber optics-based approaches is that they can lead to significant spatial distortion caused by the non-identical spatial orientation of the fiber bundles at the ends of the tapers [20], which is harder to compensate than the overall spatial distortion of classical optical components because of its non-linearity and asymmetricity (*e.g.*, [21,22]).

The PSI Neutron Microscope Project [23,24] follows a classic scintillator/mirror/lens design but adopts a bespoke, high numerical aperture lens with a fixed focal length and fixed optical magnification of about 4. The highest resolution of 4.2 μm was currently achieved at the Institut Laue Langevin [25] based on 40 individual radiographs over about 20 minutes total exposure time.

In this work we show that an infinity-corrected approach adopted for the visible-light optics [26–28] in combination with thin-film crystal scintillators can be employed to achieve similar

or even better spatial resolutions with increased detection homogeneity while retaining some flexibility concerning the optical magnification, the choice of the imaging sensor, the final nominal pixel size and the field of view.

As a result, the highest neutron imaging resolution achieved thus far (to the best of the authors' knowledge) in direct (*i.e.*, integrating) observation will be reported. This yields a resolution estimated to be as high as 2.5 µm. A key aspect of this achievement is the adoption of a thin-film *crystalline* scintillator, gadolinium gallium garnet $Gd_3Ga_5O_{12} : Eu$ (GGG:Eu), as opposed to the traditional powder scintillators.

The results presented here complement previous work [27] adopting thin-film crystalline scintillators for imaging, with a reported resolution of around 15 μm.

As will be shown, the resulting detector system allows exposure times well compatible with high quality tomographies within roughly a few hours. This opens unprecedented venues in terms of in-operando testing. In this work a tomographic acquisition of a silver based gas diffusion electrode with a nickel mesh and high porosity was performed in 10.5 hours with the same optical setup albeit at a lower resolution compared to the maximal ones obtained here in radiography, deliberately chosen to match the features of interest of the sample.

The tests were performed at NeXT-Grenoble [29,30], a novel **Ne**utron and **X**-ray **T**omograph developed at the Institut Laue-Langevin in collaboration with the Université Grenoble Alpes. This facility possesses a continuous and high cold neutron flux, which is essential for both keeping the scanning times reasonable and where (relatively slow) dynamic processes are involved.

This new detector was built at NeXT-Grenoble in collaboration with the Helmholtz-Zentrum Berlin, employing a flexible (*i.e.*, modular) and compact design, and therefore adaptable to any other neutron facility. This minimal encumbrance also enables its simultaneous use with the x-ray tomography setup available at NeXT, which can provide highly complementary information.

2. Detector

To achieve high spatial resolutions, a high degree of beam collimation (L/D, with L being the distance between the pinhole and the detector and D being the pinhole size) is usually necessary. Despite the usually smaller object sizes and thicknesses in comparison to lower spatial resolutions, the space "wasted", *e.g.*, due to substrate thicknesses, or safety clearance distances between sample and detector (or even required for sample environments), is often comparable, but constitutes then a larger fraction of the overall distance, which needs to be compensated by a lower geometric unsharpness. This higher collimation of the beam comes at the cost of a reduced neutron flux at the sample position. Also, given the smaller region of space that a pixel represents, the number of neutrons *per pixel* is further reduced.

Eventually, scintillators with high light output like the lithium-based ones cannot be employed. The spatial resolution in most current system is in fact limited by the mean free path of the charged particles produced by the neutron capture. In Li-based scintillators the capture process begins with the fission of ^{6}Li, which emits triton and alpha particles. Because of their high energy their mean free path in ^{6}Li/ZnS is 130 µm [31], which limits their resolutions to about 50 µm in practice. In gadolinium-based scintillators the neutron capture reaction emits instead conversion electrons, whose mean free path is around 12 µm. While 10 µm of Gd can capture 90 % of the neutrons, the corresponding photon production is orders of magnitude lower than for LiF scintillators. This lower light output can be compensated by a larger collection efficiency for the emitted photons *e.g.*, by increasing the numerical aperture (NA) of the objective lens to augment its solid angle coverage. The main limitation of this approach is of course the reduction of the depth of field at higher numerical apertures. This approach is then only possible by adopting scintillators such as the Gd-based ones. The uniquely high neutron attenuation of gadolinium, allows in fact to attenuate a significant fraction of the neutrons after only few µm and the vast

majority after the first 10 μm. This can become particularly important in crystalline scintillators as further detailed in section 2.2.

2.1. Infinity corrected optics

From the above considerations it follows that a high resolution detector should ideally adopt an optically optimized solution to at least partially compensate for the lower photon production per neutron of the scintillator, as well as for the limited neutron flux.

Some of the advantages of the infinity corrected optics approach in Fig. 1(b) are their modularity and flexibility in terms of distances and magnification changes, and the fact that additional optical elements can be introduced in the parallel light path (*e.g.*, filters, diaphragms) with minimised introduction of artefacts. For example, when adopting thin-film scintillators on transparent substrates, substrate luminescence may occur. With infinity-corrected optics it is possible to attenuate unwanted parts of the spectrum by simply adding a filter in the parallel light beam between objective lens and tube lens, without introducing focus shifts or additional aberrations.

The infinity corrected optics approach is widely used in modern microscope systems (operating in the visual and near-visual wavelength ranges) and has already been proposed in [26] for an x-ray scanner and adopted for neutron imaging in [27,28]. This approach employs an objective lens to capture the light emitted by the scintillator and collimate it into a parallel light path. This is then captured by a so-called tube lens (in our case a standard photographic imaging lens) to focus the image onto the sensor chip of the camera, as illustrated in Fig. 1. This allows a significant reduction of the light loss between scintillator and sensor due to the large distance between scintillator and objective lens in the traditional scintillator/mirror/lens approach.
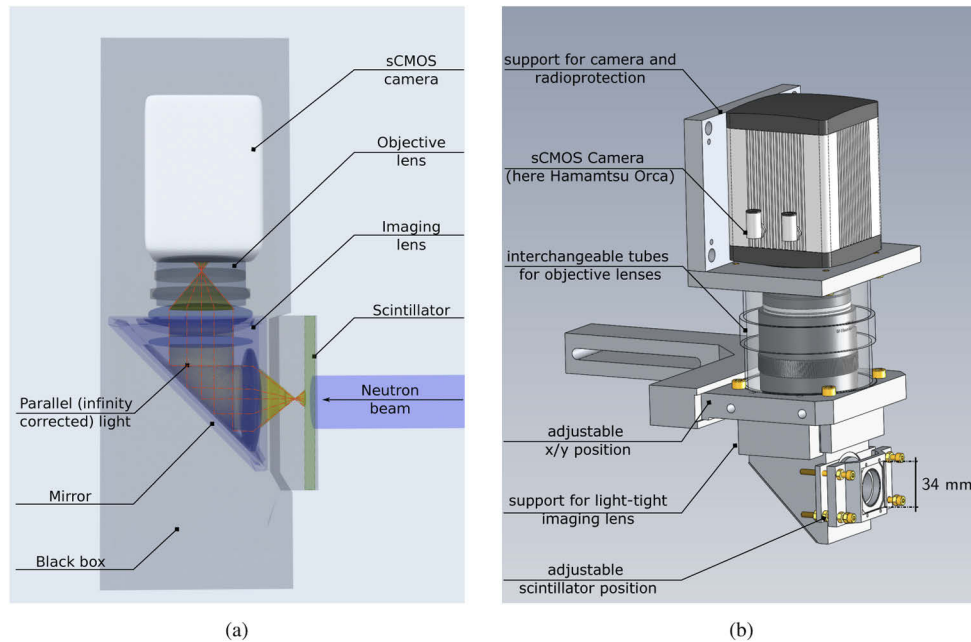

Fig. 1. Design of the high resolution detector at NeXT: (a) conceptual design, highlighting the logic of infinity corrected optics and (b) final design highlighting the minimal encumbrance and modular nature.

NeXT-Grenoble currently features three setups based on three right-angle objective lenses manufactured by Rodenstock: XR-Heliflex f = 122 mm f/2.6 (Numerical Aperture NA = 0.2), an XR-Heliflex f = 100 mm, f/1.50, (NA = 0.32) and a TV-Heliflex f = 55 mm, f/1.0, (NA = 0.41).

In infinity corrected detectors the magnification M is the ratio between the focal length of the objective lens f_I and that of the tube lens f_O: $M = f_I/f_O$. The effective pixel size P_{eff} is then simply the ratio between the true pixel size on the chip P_{chip} and the magnification: $P_{eff} = P_{chip}/M$.

For example when the 55 mm TV-Heliflex is used in combination with a 180 mm Canon tube lens, the magnification factor M is 3.27. Then, if a ZWO Camera, ASI183MM Pro is used, given its $P_{chip} = 2.4\mu m$, the resulting virtual pixel size P_{eff} is 2.4/3.27 =0.73 μm. Given its 5496x3672 pixels, this yields the *relatively* large field of view of 4.03x2.77 mm. Another camera available at NeXT is the Hamamatsu ORCA-Flash4.0 V2 sCMOS camera, which has an array of 2048x2048 pixels 6.5 μm in size, yielding a virtual pixel size of 6.5/3.27 =1.99 μm with the same lens setup, for a field of view of 4.07x4.07 mm. While the two fields of view are comparable, the ZWO ASI183MM has a pixel size nearly three times smaller which comes of course at the cost a reduced flux *per-pixel*. The ZWO ASI183MM camera is therefore used here for the determination of the attainable resolution with the thin-film scintillator, as described in Section 3.2.

Further lens couplings are reported in Table 1, while Fig. 2 reports a list of possible combinations between the three aforementioned objective lenses and some of the tube lenses available at NeXT-Grenoble (50 mm, 60 mm, 85 mm, 100 mm , and 180 mm) for the two cameras. While zoom lenses can certainly be adopted within this logic, yielding all intermediate fields of views, these lenses generally have higher distortion and chromatic aberration, lower sharpness, as well as lower numerical aperture, which increases the exposure time.
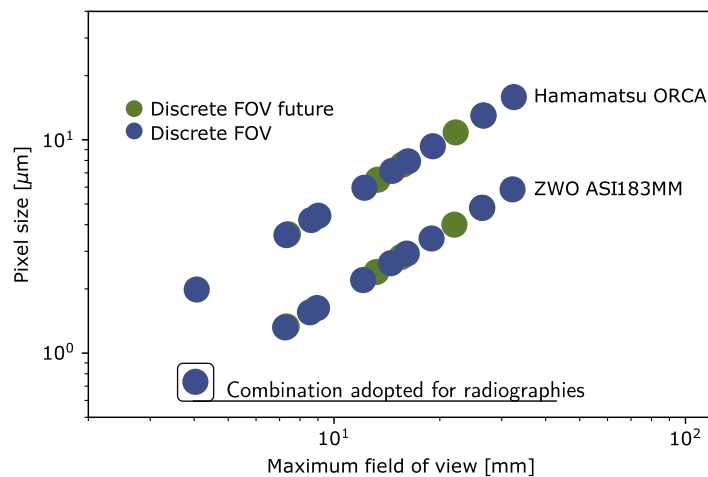

Fig. 2. Fields of views allowed by the range of infinity corrected optics currently available at NeXT-Grenoble.

Table 1. Magnification, Effective Pixel Size, and Field of View (FOV) for Several Combinations of Available Objective/Tube Lenses for the Two Available Cameras: A^*: for Hamamatsu ORCA-Flash4.0 V2 and B^{**}: for ZWO Camera, ASI183MM Pro.

Obj Lens	Img. Lens	Magnification	Pixel Size A^* [μm]	Pixel size B^{**} [μm]	FOV A^* [mm^2]	FOV B^{**} [mm^2]
50	55	0.90	7.15	2.64	14.64	14.51x9.96
100	55	1.81	3.58	1.32	7.32	7.25x4.98
180	55	3.27	1.99	0.73	4.06	4.03x2.77
50	122	0.41	15.86	5.76	32.48	31.65x21.72

This study relies on the detector mounting the 55 mm TV-Heliflex lens, whose design is reported in Fig. 1(b). The proposed design allows for tube lenses of different focal length to

be mounted while maintaining a fixed and minimal distance between the two lenses, thanks to interchangeable light-tight aluminum tubes. This is important because, while the objective lens produces a parallel light beam, the off-axis light rays, still parallel, are not collected by the tube lens. In order to minimize photon loss, this distance must be kept to a minimum. Both the aforementioned cameras can be mounted on the detector, depending on the required pixel size, field of view and efficiency.

In this kind of setup the focal point of the objective lens (*i.e.*, where the light emitting side of scintillator screen needs to be placed) is fixed. While the adjustable and motorized focus on the objective lens allows for a variation of this distance, this affects the effective focal length and reduces the sharpness as well as the numerical aperture of the lens. In this design the scintillator position is also adjustable in order to maximize image quality.

The minimization of the scintillator/sample distance is also favoured by the minimal encumbrance of any non-essential component (*e.g.*, the body of the Heliflex is not further wrapped in a box, being already light tight. This compactness is also important to minimize any mechanical interaction with the x-ray setup available at NeXT-Grenoble. This is further helped by the possibility to orient the detector in three different positions (with camera to the right, the left or above the beam).

2.2. Scintillating screen

A central aspect in the detection of neutrons is the scintillator. Given the finite number of neutrons per second impacting it, the signal exhibits an intrinsic "shot noise", which can be described through a Poissonian distribution (which morphs into a Gaussian distribution as the flux increases). Its average is the average number of neutrons N, whereas its standard deviation is $\sqrt{N}$, meaning that the signal-to-noise ratio SNR = $N/\sqrt{N} = \sqrt{N}$. These "neutron statistics" correspond to a given "photon statistics", which depend on the kind of scintillator screen used. The overall quality of the image is a function of both neutron and photon statistics. While improved neutron statistics improve image quality (although at a decreasing rate), there comes a point when an improvement in photon statistics is nearly uninfluential on the image quality.

Given the fixed maximum flux at a given source for a given collimation L/D, the simplest path to improve signal statistic is to adopt longer exposure times. This comes nonetheless at the higher likelihood of unwanted high energy gammas (*e.g.*, produced by the gadolinium in the scintillator) hitting the chip of the camera, causing noise (in the form of white spots) which pollutes the image quality. Also the dark currents of the camera will increase with increased exposure. To optimize the ultimate image quality all these factors should be taken into account.

As aforementioned, the mean free path of the tritium particles in lithium-based scintillators is incompatible with higher resolutions. The free mean path of the conversion electrons used in gadolinium-based scintillators is instead one order of magnitude lower than that of tritium, more compatible with higher resolutions. The typical gadolinium-based scintillators for neutron imaging applications are powder-based. One of the main shortcomings of powder-based scintillators is the photon scattering at the grain surfaces (Fig. 3(a, b)). If the screen thickness increases in fact, the higher likelihood of scattering decreases the spatial resolution (following a Lambertian distribution), which ends up being approximately equal to the thickness of the scintillator itself ([32,33]). Thinner scintillators are well known (*e.g.*, [34,35]) to be better suited for higher resolutions. Nonetheless, while 10 μm of gadolinium can stop more than 90 % of the beam, at, for example, 3.5 μm the captured flux is closer to 50 %. To circumvent this issue the isotope 157 of gadolinium can be employed. In the cold neutron spectrum its cross section is about five times higher than that of the natural gadolinium (which contains only about 15.6 % of the 157 isotope). A family of scintillators with higher 157-isotope content ($^{157}Gd_2O_2S : Tb$) is described in [36]. These scintillators are optimised for high-resolution neutron imaging and were adopted in previous high resolution achievements (*e.g.*, [24,25]). A 3.5 μm thick 157-Gd

scintillator of this category was also used in this work and serves as reference for the crystalline scintillator, which is the focus of this work.
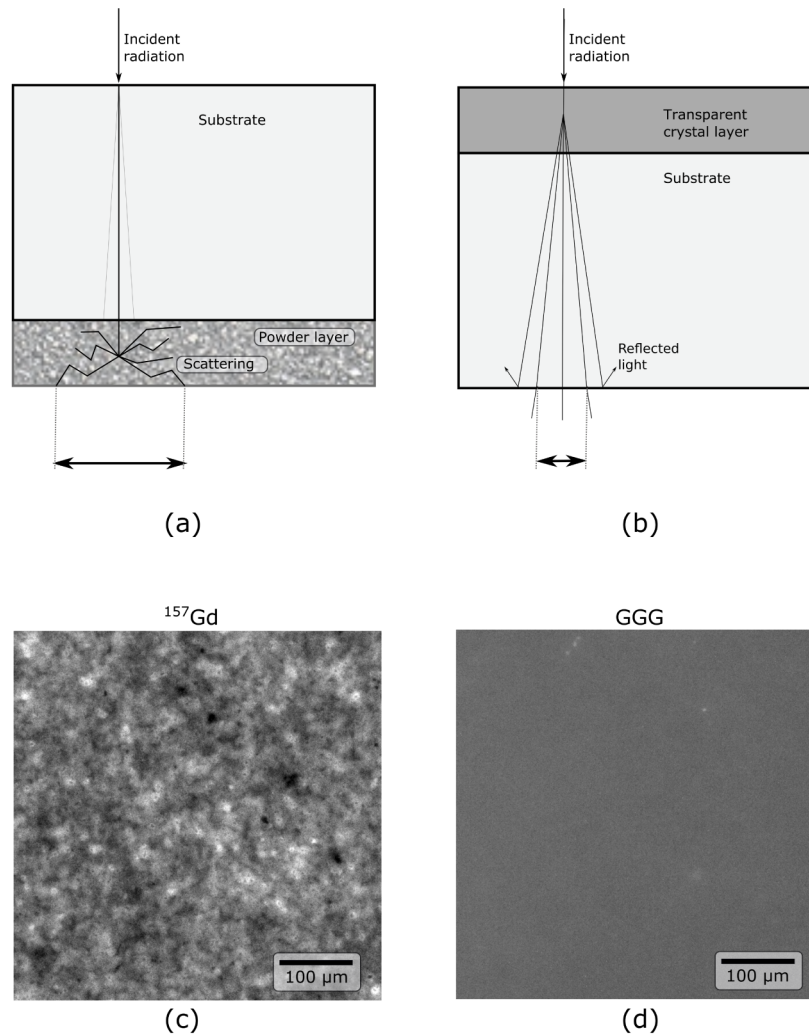

Fig. 3. Comparison between powder screen (left) and the single crystal one (right). Top row: conceptual difference in the light emission and transport in (a) powder and (b) transparent thin layer scintillators, adapted from [37]. Bottom row, (c) homogeneity of the light output in a 157-Gd scintillator and (d) in a GGG one, as produced when exposed to the same neutron beam, and shown here with the same contrast, of about 2000 counts, post dark-field corrections. It should be noted that the substrate for the former is generally aluminium or glass, and is placed in between the powder and the sample as support and protection. In thin film scintillators, the support is in general a layer of transparent, non-doped crystal. Since this layer is still attenuating it makes more sense to have the doped layer towards the neutron source instead.

In powder scintillators, the minimum size of the grains ultimately defines the lower boundary of the thickness and therefore the resolution. In gadolinium powder-based scintillators, the particle size averages about $2\,\mu m$ (*e.g.*, [36]), which poses a significant limit to the approach. Additionally, as the powder layer gets finer, the surface becomes progressively less homogeneous, resulting in a higher variation of the neutron and photon statistics and thus of the resolution

across the scintillator surface as shown in Fig. 3(c, d). In X-ray applications, for these class of scintillators two to three layers of phosphor grains are generally employed to tackle this issue [33].

The scattering at the grain boundaries of powder-based scintillators is one of the key reasons that pushed the x-ray community towards a different category of scintillators made of single crystals. In this case the light travels to the surface with less scattering, reducing the blurring and increasing photon transmission, thanks to the transparency of the crystal. Furthermore only the fraction of light below the critical angle can exit the scintillator, as highlighted in Fig. 3(b). In this case the thickness of the active layer has a smaller effect on the light scattering and the limitation posed by the fact that the scintillator thickness equals the maximum attainable resolution is removed. The main effect that the crystal thickness has on the resolution concerns, in fact, the optics employed and their aperture, which determine the depth of field in focus, as aforementioned. A variety of compounds are routinely used in x-ray imaging (*e.g.*, LSO, LuAG, YAG). For neutron imaging one is of particular interest: Eu- or Tb-doped gadolinium gallium garnet $Gd_3Ga_5O_{12}$. The high neutron attenuation power of gadolinium can in this context be taken advantage of, to adopt high numerical aperture lenses to collect a large fraction of the light emitted without penalising spatial resolution.

For example, at a wavelength of about 2.6 Å, a 30 μm thick GGG crystal absorbs roughly 93% of the incoming neutrons (*i.e.*, a transmission $T \approx 7$ % for the purple line in Fig. 4 (a)). Neglecting in first approximation the decay of the number of neutrons absorbed along the beam direction as well as light scattering effects (and assuming circular entrance pupils in the optical imaging system), the attainable spatial resolution has two major contributions [38,39]: one given by the diffraction limit of the objective lens, the other being the defect of focus inside the finite crystal thickness. For more details, the reader is referred to the literature, see *e.g.*, the thesis of F. Riva [40]. From Fig. 4 (b) it can be observed how, adopting the coefficients calculated by [38], the system is diffraction-limited for low numerical aperture values, *i.e.*, almost no resolution gain would result from further thinning the conversion screen (the purple line in Fig. 4 (b), which is almost horizontal). On the other hand, for large NA values >0.5 significant resolution gains can still be attained for crystal thicknesses towards 1 μm (*e.g.*, the light yellow line).
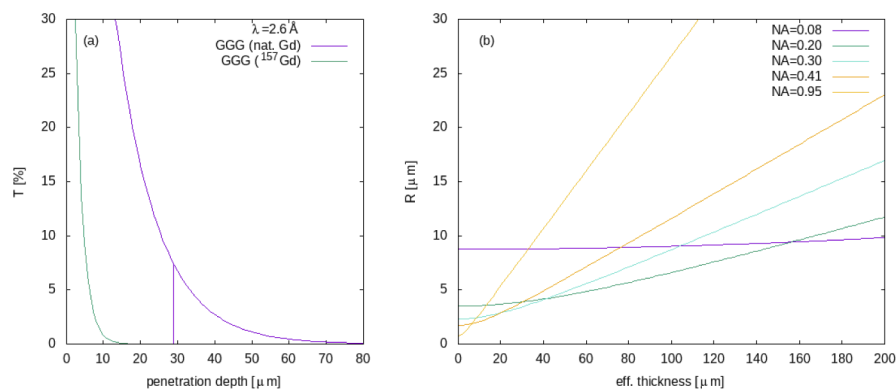

Fig. 4. Transmission T as a function of penetration depth (a) for a neutron wavelength $\lambda =$ 2.6 Å into an ideal GGG crystal (purple line for natural Gd and green line for a hypothetical ^{157}Gd-enriched crystal) along with a numerical analysis (b) of the attainable spatial resolution R, depending on the effective thickness of the translucent crystal, and for different numerical aperture (NA) values of the objective lens (derived from [38]).

The optimal point for sub-5 μm resolution with realistic optics between NA=0.4 and NA=0.2 corresponds to an effective thickness of approximately 30 to 40 μm, which is larger than the

thickness of the scintillator adopted in this work. This should allow for attaining optimal focusing with the chosen optics without loss of resolution caused by the finite scintillator thickness.

More specifically, for the selected objective lens limited by a numerical aperture of 0.41 (orange line in Fig. 4 (b)), we can observe that it is possible to attain a spatial resolution well below 5 μm, despite the hypothesis of a "worst-case scenario " that light conversion is uniform along the crystal thickness. Since, in reality, 70 % of the neutrons are likely already absorbed in the first 10 μm of the crystal, the effective crystal thicknesses is actually much smaller and better spatial resolution can be expected due to a reduced effective defect of focus along the optical axis. Considering now the possible development of an isotope-enriched (^{157}Gd) GGG scintillator material, this effective thickness could be further reduced by a factor of -indicatively- five (green line in Fig. 4 (a)), based on the aforementioned hypotheses. This would result in an even higher spatial resolution, assuming that no further resolution-degrading effects need to be considered. It should be noted that, since light is transmitted (and observed) through a transparent substrate, refraction in practice limits the NA_{eff} to ≈0.2 according to Snell's law, for an air-coupled objective lens with a nominal NA=0.41.

To date, single-crystal scintillators are the preferred approach for sub-μm *detector* resolution in synchrotron imaging [37,40,41]. These properties of single crystal scintillators have been thoroughly studied in high resolution synchrotron x-ray imaging, and are likely to be applicable also to high resolution neutron imaging.

Both GGG and the aforementioned gadox undergo a similar neutron-to-photon process, which relies on the intermediary electron conversion, with a mean free path of approximately 10-20 μm. Several scintillators coming from the Instrument Support and Development Division, Detector Unit at the European Synchrotron Radiation Facility (ESRF) were tested in this work, and the measured light outputs are summarised in Table 2. These differences can be justified by the different thicknesses and growth rates, which can introduce different amounts of impurities in the layers (for example the Platinum coming from the crucible or the lead coming from the solvent used for the liquid phase epitaxy). In these scintillators, a thin layer of $Gd_3Ga_5O_{12}$ doped with Eu^{3+}, produced by liquid-phase epitaxy lays on a pure of $Gd_3Ga_5O_{12}$ substrate. Amongst them, the scintillator marked as Z21 was chosen in this work for the determination of the resolution detailed in the next section for its combination of homogeneity and light output. It has a 29 μm thick active layer, which, for synchrotron imaging, is normally compatible with sub-μm resolutions [40]. The scintillator emission spectrum for this kind of scintillators is reported to have two main peaks around 595 nm and 710 nm when excited by 8 keV radiation. While the excitation processes for x-ray radiation significantly differs from the neutron one, the characteristic emission is a function of the electronic properties of the Eu^{3+} dopant. Excitation induced by x-ray or neutron capture conversion electrons should produce similar emission spectra, which matches well the quantum efficiency response of the used sCMOS.

Table 2. Comparison of the Photon Flux Generated by a Range of GGG Scintillators. All these scintillators come from the same bath and have the same chemical composition. It should be noted that all these GGG:Eu scintillators present an active layer on both faces of an undoped GGG substrate (indicatively 0.5 mm thick). *Flux in arbitrary units, camera counts.

Code	Flux*, Face 1	Flux* Face 2	Features
Z32	770	770	GGG:Eu, 46 μm, 0.77 μm/min growth
Z19	930	910	GGG:Eu, 58.9 μm, 0.59 μm/min growth
Z21	860	850	GGG:Eu, 29 μm, 0.49 μm/min growth
Z29	870	860	GGG:Eu, 59 μm, 0.92 μm/min growth

The light output of the chosen scintillator (Z21) compares positively with the reference powder-based scintillator for high resolution, the 3.5 μm screen enriched with 157-Gd. While the latter is optimised for high resolution neutron imaging, in fact, the GGG scintillator, which was optimised for x-ray imaging, has only about 35 % less light output. It is likely that single crystal scintillators will yield as much as, or even more light than, the powder ones, when employing 157-Gd and following optimisation for neutron applications. The crystal screen also provides a more homogenous illumination, as highlighted in Fig. 3, which should yield more consistent statistics and resolution throughout the field of view. Finally, and most importantly, the maximum resolution of single crystal scintillators is not equal to their thickness, as in powder-based ones, thanks to the reduced scattering. Section 3.2 attempts to determine the resolution attainable by the chosen single crystal scintillator.

3. Results

3.1. Testing conditions at NeXT-Grenoble

The detector was tested at NeXT-Grenoble, the recently developed Neutron and X-ray Tomograph installed at the Institut Laue-Langevin [29,30] in collaboration with the Université Grenoble Alpes. This facility currently provides the highest cold neutron flux for imaging purposes in the world. NeXT-Grenoble is at the end of a curved m=2 neutron guide with a maximum radius of 4 km, to reduce unwanted epithermal and fast neutrons as well as gamma radiation which would derive from a direct view on the reactor. The neutron spectrum peaks at 2.8 Å, as highlighted in Fig. 5. At the end of the guide the flux is 1.4×10^{10} n/cm^2/s. The tomograph itself is placed at 10 m from a selector of circular pinholes ranging from 1.5 to 30 mm.
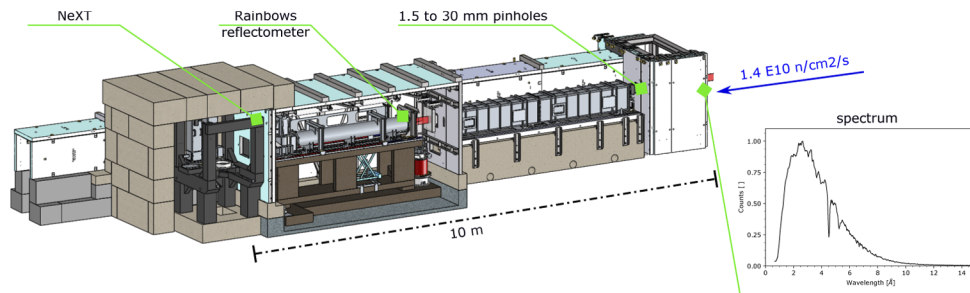

Fig. 5. 3D scheme of the NeXT-Grenoble tomograph, placed 10 meters after a set of pinholes ranging up to 30 mm. On the left the image reports the flux at the pinhole as well as the spectrum of the beam.

In order to measure the spatial resolution of our detector system in highly oversampled conditions we coupled the Canon f = 180 mm f/3.5 tube lens with the TV-Heliflex f = 55 mm, f/1.0 objective lens, giving a magnification factor M of 3.27. This is combined with the ZWO ASI183MM which provides an estimated virtual pixel size 0.73 μm. Using targets of known geometry we measured a pixel size of 0.75 μm, a 3% difference compatible with the range of variation induced by focussing. In the following, the larger, measured, pixel size will be used, which is the conservative approach in terms of maximum attainable resolution. The detector mounts the aforementioned Z21 GGG scintillator.

In this example a relatively high collimation was chosen to minimise the geometrical blurring, by combining a 15 mm pinhole with a 10 m pinhole/detector distance, resulting in a collimation ratio of 667. The optical targets were placed at about 0.2 mm from the scintillator, yielding a maximum geometric blurring $d \sim D/L \times l = 0.3 \mu m$ This is not the highest flux that this beamline can provide (which is attainable at 5 m for a 30 mm pinhole), but still provides a flux of

about 8×10^7 n/cm^2/s, *i.e.*, 0.6 n/pixel /s, yielding approximately 2200 greylevel counts per pixel over a 60 seconds exposure. This corresponds to a count rate of 36 counts /pixel /s, and thus a count/neutron ratio of about 60.

3.2. Analysis of resolution

Firstly, the optical resolution of the setup was assessed using a 1951 USAF Resolution Test Target. As highlighted in Fig. 6, the spokes of Element 6 in Group 7 are clearly visible (the highest available in this version of the target), which suggests a resolution of at least 2.19 μm can be achieved optically with this setup.
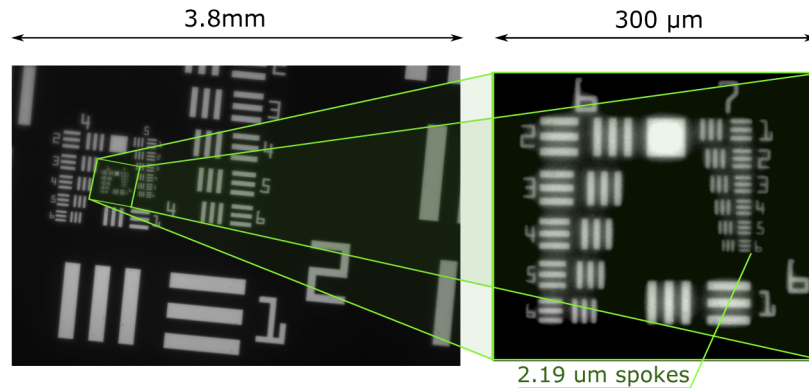

Fig. 6. Optical resolution, as obtained by 1951 USAF Resolution Test Target, demonstrating that an optical resolution of at least 2.19 µm can be achieved.

To assess the "neutron" resolution, a Siemens star pattern [42] was used as a target. Fig. 7 reports a representative radiography of the Siemens star, obtained by taking the median of 13 acquisitions, corresponding to a 13 minutes overall exposure at a collimation ration L/D of 667. The 4 µm thick spokes of the target are clearly visible, indicating a resolution below 4 µm.
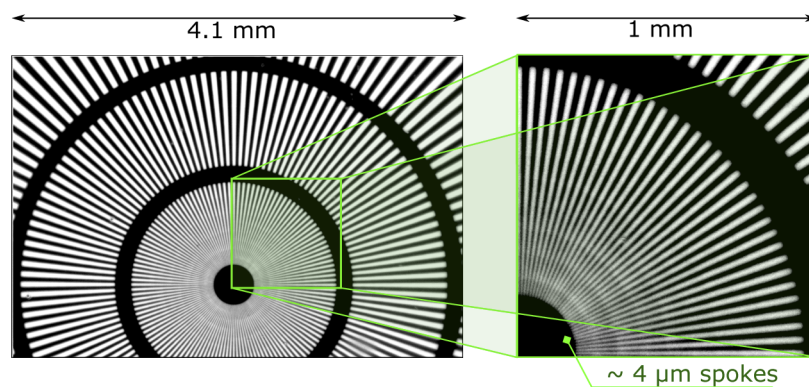

Fig. 7. Radiography of a Siemens star target, resulting from the medianing of 13 radiographies. In the zoomed-in sub-picture to the right, the 4 µm spokes are visible.

To further assess then the neutron resolution of the detector, multiple approaches were undertaken. One of the reference methods to assess resolution is through the analysis of the Modulation Transfer Function (MTF) of a highly absorbing slanted edge, which assesses the loss of contrast of the imaging system as a function of the spatial frequency [43,44]. A threshold of

8.95% on the contrast level (often approximated to 10%) is generally employed, which can be proven to correspond to the Rayleigh Criterion. This method is often employed in neutron and Synchrotron imaging (*e.g.*, [45,46]). One of the underlying hypotheses of this approach is that a sharp, highly absorbing material is used. Several gadolinium foils of thicknesses varying from 100 μm to 20 μm were tested in this work but they all presented significant imperfections in the order 10 μm and above, far too high for MTF analysis at this resolution. In synchrotrons, cleaved crystals are generally used to have a sharp (few atoms thick) boundary to determine resolutions around the micron, *e.g.*, using 500 μm GaAs [33], whose transversal orientation to the scintillator plane is also typically optimised. In neutron imaging the equivalent approach has not, to the best of the authors' knowledge, been found yet.

The edge of a spoke of the siemens star itself was therefore employed in this work. This target is created by etching a 6 μm layer of gadolinium, which means that, while the edges can be sharp, the contrast is quite low (about 50 %), which is far from the ideal conditions for MTF evaluation. The result of the the analysis of this edge gives a resolution below $4\mu m$, although given the low contrast this should be interpreted as an *upper boundary* of the true resolution.

Another Technique which is increasingly used in x-ray [47] and neutron [24] imaging applications is Fourier Ring Correlation (FRC) [48]. This method measures the normalized cross-correlation coefficient between two independently acquired images over a ring in Fourier space (*i.e.*, as a function of spatial frequency). The choice of the correct threshold to determine the image resolution is still somewhat open to debate. Here we used the fixed-value threshold method [49] which was proposed to make the results consistent with cryo-EM reconstructions. As shown in Fig. 8 the deduced resolution can be estimated to be as low as 2.5 μm in as few as 10 images. Alternative threshold method have also been tested all coherently revealing resolutions below 4 μm for a comparable number of images.
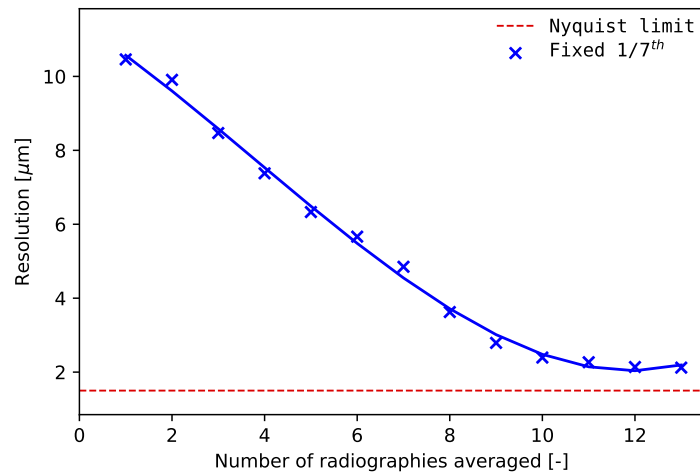

Fig. 8. Resolution of the setup derived from the Fourier Ring Analysis as a function fo the number of radiographies averaged. This reveals a maximum resolution around 2.5 μm with a fixed $1/7^{th}$ method. The radiographies used were in this case of the Siemens Star target.

Irrespective of the exact numerical value of the resolution, all methods agree that the proposed approach improves over the current record which is at 4.5 μm, getting to a resolution somewhere between 4 μm (from the upper-boundary MTF) and 2.5 μm, depending on the approach. This is also confirmed by optical analyses, the observations on the Siemens Star as well as from theoretical considerations on the essential elements influencing the resolution (scintillator technology, optics, collimation). It is the authors' opinion that for consistency with the existing neutron literature an ideal way forward is through the further extension of the lower boundary of the Siemens

Star and/or by evaluating the MTF adopting a cleaved crystal of a material with high neutron attenuation, and will be the focus of future work.

It should also be noted that the relatively high collimation ratio used could be reduced with moderate influence on the resolution, *e.g.*, a collimation of 332 could be adopted with an expected geometrical blurring of 0.6 µm and for times more flux.

One the advantages of the proposed *optical* setup is that when combined with the flux available at NeXT-Grenoble, the scanning time becomes compatible with correspondingly high resolution tomography.

Furthermore, this setup is highly flexible, allowing for the rapid change to the fields of view in Fig. 2. The tomographic compatibility of the setup is explored more in detail in the example in the next section.

4. Representative tomographic application

One of the key applications of high resolution neutron imaging is the study of energy materials. Fig. 9 shows a silver based gas diffusion electrode (GDE), which is applied at oxygen depolarized cathode technology in chlor-alkali electrolysis. The application of oxygen depolarized cathodes is a novel concept, which leads to significant energy savings and reduction of CO_2 emission when compared to the more commonly used hydrogen evolving cathodes [50,51]. These GDEs exhibit a complex microstructure with a highly branched pore system in a silver grain scaffold, in which phase boundaries are coated with polytetrafluorethylene [52]. Within the GDEs there is a Ni mesh, which supports the electric conductivity.
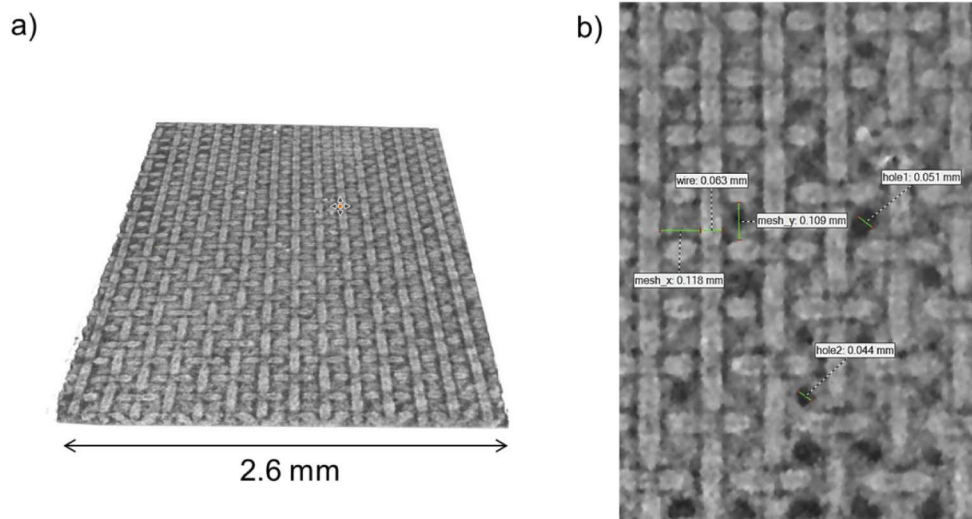

Fig. 9. Silver based gas diffusion electrode, which contains a nickel mesh, a) high-resolution tomography, b) slice, showing pores within the silver and between the nickel mesh.

To understand the electrochemical processes, the understanding of this complex microstructure is of pivotal importance, and high resolution neutron tomography lends itself as an ideal probing tool. The neutron tomography in Fig. 9 reveals pores 20 to 50 µm in diameter within the silver as well as between the nickel wires. In a next step, operando measurements are planned to observe the spreading of the hydrogen-rich electrolyte ([53,54]). The high contrasts between nickel/silver and hydrogen allowed by high resolution neutron tomography opens unprecedented possibilities in the study of GDEs.

To capture this, the setup detailed in Section 3.2 was employed in binning 2, yielding a virtual pixel size around 1.5 µm. 636 individual projections, each the result of the median of three 20-second long projections comprise this ~ 10.5 hour long tomography. The sample is about 2.6 mm wide, and was placed vertically with a distance to the scintillator in the order of 2.8 mm. The 15 mm pinhole was used, which, combined with the 10 m distance yields a maximum geometric blurring d ~ D/L*l= 15 mm /10 000 mm * (2.8 mm)= 4.2 µm, well compatible with the radiographic resolution and the features of interest.

This proves the high efficiency and flexibility of the setup and its value for high resolution applications, such as energy materials.

In order to reduce the statistical noise, a TVmin [55] filter was applied to the normalized projections. The parameters of this filter were optimized by analyzing the result of the subtraction between the original and the filtered images, and specifically choosing the set showing only statistical noise. The tomographic reconstruction was obtained through a standard filtered-backprojection algorithm (FBP) for parallel beam. The reconstructed slices were filtered by a 3D Non-Local Mean (NLM) filter [56]. The 3D rendering and the analysis of the tomographic data were made with the help of Volume Graphics StudioMax software.

It should be noted that, in order to maximise resolution up to the values determined in the previous paragraphs for radiography, the tomography should be acquired without binning, and should comprise enough projections to respect Nyquist's sampling theorem. Furthermore, for samples of this size, a higher collimation would be necessary. While the parameters used were sufficient to capture the features of interest in this case, all of these refinements to attain maximal resolution would of course imply a longer overall acquisition time.

5.　Discussion and conclusion

This paper presents the potential of single-crystal thin-film scintillators in combination with infinity corrected optics for high resolution neutron imaging. The infinity corrected approach is one of the reference approaches in synchrotron imaging with engineered detector systems readily available [57], while it's far less common in neutron imaging. Coupled with a novel slim and flexible design makes this compact detector ideal for simultaneous x-ray and neutron studies as well as for in-situ testing. Additionally, this approach is rather cost effective and can be easily adopted at virtually any beamline.

Single crystal scintillators are perhaps the reference solution for sub-μm detector resolutions in synchrotron imaging. In neutron imaging only very little is documented about this approach, with only one major publication [27] at significantly lower resolutions. In this work, the viability and efficiency of a set of scintillators made of Eu-doped gadolinium gallium garnet $Gd_3Ga_5O_{12}$ was tested and found to compare positively to a reference [157]Gd-enriched gadox (gadolinium oxisulfide) powder scintillator optimised for high resolutions. This opens new venues for high resolution neutron imaging thanks to the advantages of single crystal scintillators, which remove the limits dictated by the thickness of powder scintillators, and their spatial heterogeneity.

The combination of the optical setup and scintillation approach allowed for unprecedented sub-4 µm true resolution. Multiple methods (Siemens star target, modulation transfer function, Fourier ring correlation) as well as optical verification and theoretical considerations agree on the sub-4 µm resolution although some suggest that it may well be as low as 2.5 µm. Regardless of the exact numerical value, this approach appears very promising. It is envisaged that the development of resolution evaluation methods similar to the synchrotron ones (MTF of a sharp cleaved edge of a highly absorbing crystal) as well as the extension of the Siemens Star to higher resolutions will help further refine the assessment of the attainable resolutions of this and other setups.

The short acquisition times, also made possible by the flux at NeXT-Grenoble, allow the acquisition of high resolution tomographies, as exemplified by the acquisition of a silver based

gas diffusion electrode with a nickel mesh and high porosity. This tomography was acquired in less than 11 hours at a resolution optimised for its $\sim 5/10\,\mu$m features.

This opens new venues in the domain of neutron imaging, rendering high resolution imaging more enticing for a number of open scientific questions, ranging from in-situ testing of commercial fuel cells to in-situ testing of lithium batteries, to mention only a few.

Disclosures. The authors declare no conflicts of interest.

Data availability. Data underlying the results presented in this paper are available upon request to the authors.

References

1. B. Winkler, "Applications of neutron radiography and neutron tomography," Rev. Mineral. Geochem. **63**(1), 459–471 (2006).
2. J. Banhart, A. Borbély, K. Dzieciol, F. Garcia-Moreno, I. Manke, N. Kardjilov, A. R. Kaysser-Pyzalla, M. Strobl, and W. Treimer, "X-ray and neutron imaging–complementary techniques for materials science and engineering: Dedicated to professor dr. h.-p. degischer on the occasion of his 65th birthday," Int. J. Mater. Res. **101**(9), 1069–1079 (2010).
3. N. Kardjilov, I. Manke, A. Hilger, M. Strobl, and J. Banhart, "Neutron imaging in materials science," Mater. Today **14**(6), 248–256 (2011).
4. N. Kardjilov, I. Manke, R. Woracek, A. Hilger, and J. Banhart, "Advances in neutron imaging," Mater. Today **21**(6), 652–672 (2018).
5. A. Tengattini, N. Lenoir, E. Andò, and G. Viggiani, "Neutron imaging for geomechanics: a review," Geomech. for Energy Environ. **27**, 100206 (2021).
6. D. Liu, D. Hussey, M. Gubarev, B. Ramsey, D. Jacobson, M. Arif, D. Moncton, and B. Khaykovich, "Demonstration of achromatic cold-neutron microscope utilizing axisymmetric focusing mirrors," Appl. Phys. Lett. **102**(18), 183508 (2013).
7. D. S. Hussey, J. M. LaManna, E. Baltic, and D. L. Jacobson, "Neutron imaging detector with 2 um spatial resolution based on event reconstruction of neutron capture in gadolinium oxysulfide scintillators," Nucl. Instruments Methods Phys. Res. Sect. A: Accel. Spectrometers, Detect. Assoc. Equip. **866**, 9–12 (2017).
8. A. Losko, Y. Han, B. Schillinger, A. Tartaglione, M. Morgano, M. Strobl, J. Long, A. Tremsin, and M. Schulz, "New perspectives for neutron imaging through advanced event-mode data acquisition," Sci. Rep. **11**(1), 21360 (2021).
9. P. Boillat, D. Kramer, B. Seyfang, G. Frei, E. Lehmann, G. Scherer, A. Wokaun, Y. Ichikawa, Y. Tasaki, and K. Shinohara, "In situ observation of the water distribution across a pefc using high resolution neutron radiography," Electrochem. Commun. **10**(4), 546–550 (2008).
10. M. Arif, D. L. Jacobson, D. S. Hussey, and N. Garland, "Neutron imaging study of the water transport in operating fuel cells," DOE Hydrogen Program FY 2010 Annual Progress Report pp. 686–692 (2010).
11. O. Siegmund, A. Tremsin, J. Vallerga, and J. McPhate, "Microchannel plate cross-strip detectors with high spatial and temporal resolution," Nucl. Instruments Methods Phys. Res. Sect. A: Accel. Spectrometers, Detect. Assoc. Equip. **610**(1), 118–122 (2009).
12. A. Tremsin, M. Morgano, T. Panzner, E. Lehmann, U. Filgers, J. Vallerga, J. McPhate, O. Siegmund, and W. Feller, "High resolution neutron imaging capabilities at boa beamline at paul scherrer institut," Nucl. Instruments Methods Phys. Res. Sect. A: Accel. Spectrometers, Detect. Assoc. Equip. **784**, 486–493 (2015).
13. M. Matsubayashi, A. Faenov, T. Pikuz, Y. Fukuda, Y. Kato, R. Yasuda, H. Iikura, T. Nojima, and T. Sakai, "Lif crystals as high spatial resolution neutron imaging detectors," Nucl. Instruments Methods Phys. Res. Sect. A: Accel. Spectrometers, Detect. Assoc. Equip. **651**(1), 90–94 (2011).
14. M. Matsubayashi, A. Faenov, T. Pikuz, Y. Fukuda, and Y. Kato, "Neutron imaging of micron-size structures by color center formation in lif crystals," Nucl. Instruments Methods Phys. Res. Sect. A: Accel. Spectrometers, Detect. Assoc. Equip. **622**(3), 637–641 (2010).
15. A. Faenov, M. Matsubayashi, T. Pikuz, Y. Fukuda, M. Kando, R. Yasuda, H. Iikura, T. Nojima, T. Sakai, M. Shiozawa, and Y. Kato, "Lithium fluoride crystal as a novel high dynamic neutron imaging detector with microns scale spatial resolution," Phys. Status Solidi C **9**(12), 2231–2234 (2012).
16. D. Vavrik, M. Holik, J. Jakubek, M. Jakubek, V. Kraus, F. Krejci, P. Soukup, D. Turecek, J. Vacik, and J. Zemlicka, "Modular pixelated detector system with the spectroscopic capability and fast parallel read-out," J. Instrum. **9**(06), C06006 (2014).
17. F. Krejci, J. Zemlicka, J. Jakubek, J. Dudak, D. Vavrik, U. Köster, D. Atkins, A. Kaestner, J. Soltes, L. Viererbl, J. Vacik, and I. I. Tomandl, "Development and characterization of high-resolution neutron pixel detectors based on timepix read-out chips," J. Instrum. **11**(12), C12026 (2016).
18. M. Matsubayashi and K. Soyama, "Preliminary examination of a ccd camera with a scintillator coated fiber optic plate for neutron imaging," Nucl. Instruments Methods Phys. Res. Sect. A: Accel. Spectrometers, Detect. Assoc. Equip. **529**(1-3), 384–388 (2004).
19. M. Morgano, P. Trtik, M. Meyer, E. Lehmann, J. Hovind, and M. Strobl, "Unlocking high spatial resolution in neutron imaging through an add-on fibre optics taper," Opt. Express **26**(2), 1809–1816 (2018).

20. G. R. Davis and J. C. Elliott, "Scintillator to ccd coupling in x-ray microtomography," in *Developments in X-Ray Tomography V*, vol. 6318 (International Society for Optics and Photonics, 2006), p. 631817.

21. M. S. Islam, R. Lewis, K. Uesugi, and M. Kitchen, "A high precision recipe for correcting images distorted by a tapered fiber optic," J. Instrum. **5**(09), P09008 (2010).

22. W. Paciorek, M. Meyer, and G. Chapuis, "Geometric distortion corrections for fiber-optic tapers in x-ray charge-coupled-device detectors," J. Appl. Crystallogr. **32**(1), 11–14 (1999).

23. P. Trtik, J. Hovind, C. Grünzweig, A. Bollhalder, V. Thominet, C. David, A. Kaestner, and E. H. Lehmann, "Improving the spatial resolution of neutron imaging at paul scherrer institut–the neutron microscope project," Phys. Procedia **69**, 169–176 (2015).

24. P. Trtik and E. H. Lehmann, "Progress in high-resolution neutron imaging at the paul scherrer institut-the neutron microscope project," in *Journal of Physics: Conference Series*, vol. 746 (IOP Publishing, 2016), p. 012004.

25. P. Trtik, M. Meyer, T. Wehmann, A. Tengattini, D. Atkins, E. Lehmann, and M. Strobl, "Psi 'neutron microscope' at ill-d50 beamline - first results," *WCNR-11 proceedings*.

26. B. R. Müller, A. Lange, M. Harwardt, M. P. Hentschel, B. Illerhaus, J. Goebbels, J. Bamberg, and F. Heutling, "X-ray refraction topography and computed tomography for nde of lightweight materials (keynote paper)," in *Testing, Reliability, and Application of Micro-and Nano-Material Systems III*, vol. 5766 (International Society for Optics and Photonics, 2005), pp. 1–9.

27. S. Williams, A. Hilger, N. Kardjilov, I. Manke, M. Strobl, P. Douissard, T. Martin, H. Riesemeier, and J. Banhart, "Detection system for microimaging with neutrons," J. Instrum. **7**(02), P02014 (2012).

28. I. Manke, C. Hartnig, M. Grünerbel, W. Lehnert, N. Kardjilov, A. Haibel, A. Hilger, J. Banhart, and H. Riesemeier, "Investigation of water evolution and transport in fuel cells with high resolution synchrotron x-ray radiography," Appl. Phys. Lett. **90**(17), 174105 (2007).

29. A. Tengattini, D. Atkins, B. Giroud, E. Ando, and B. J G. Viggiani, "Next-grenoble, a novel facility for neutron and x-ray tomography in grenoble," *Proceedings of ICTMS2017-163* **88** (2017).

30. A. Tengattini, N. Lenoir, E. Ando, B. Giroud, D. Atkins, G. Beaucour, and V. Gioacchino, "Next-grenoble, the neutron and x-ray tomograph in grenoble," Submitted.

31. C. Schulz, "Entwicklung eines neuartigen niederdruck-detektors mit hoher orts-und flugzeitauflösung zum nachweis thermischer neutronen," Ph.D. thesis (2000).

32. R. K. Swank, "Calculation of modulation transfer functions of x-ray fluorescent screens," Appl. Opt. **12**(8), 1865–1870 (1973).

33. T. Martin and A. Koch, "Recent developments in x-ray imaging with micrometer spatial resolution," J. Synchrotron Radiat. **13**(2), 180–194 (2006).

34. N. Kardjilov, M. Dawson, A. Hilger, I. Manke, M. Strobl, D. Penumadu, F. Kim, F. Garcia-Moreno, and J. Banhart, "A highly adaptive detector system for high resolution neutron imaging," Nucl. Instruments Methods Phys. Res. Sect. A: Accel. Spectrometers, Detect. Assoc. Equip. **651**(1), 95–99 (2011).

35. S. Baechler, N. Kardjilov, M. Dierick, J. Jolie, G. Kühne, E. Lehmann, and T. Materna, "New features in cold neutron radiography and tomography: Part i: Thinner scintillators and a neutron velocity selector to improve the spatial resolution," Nucl. Instruments Methods Phys. Res. Sect. A: Accel. Spectrometers, Detect. Assoc. Equip. **491**(3), 481–491 (2002).

36. P. Trtik and E. H. Lehmann, "Isotopically-enriched gadolinium-157 oxysulfide scintillator screens for the high-resolution neutron imaging," Nucl. Instruments Methods Phys. Res. Sect. A: Accel. Spectrometers, Detect. Assoc. Equip. **788**, 67–70 (2015).

37. H. Graafsma and T. Martin, "Detectors for synchrotron tomography," Advanced Tomographic Methods in Materials Research and Engineering pp. 2t77–302 (2008).

38. A. Koch, C. Raven, P. Spanne, and A. Snigirev, "X-ray imaging with submicrometer resolution employing transparent luminescent screens," J. Opt. Soc. Am. A **15**(7), 1940–1951 (1998).

39. M. Stampanoni, G. Borchert, P. Wyss, R. Abela, B. Patterson, S. Hunt, D. Vermeulen, and P. Rüegsegger, "High resolution x-ray detector for synchrotron-based microtomography," Nucl. Instruments Methods Phys. Res. Sect. A: Accel. Spectrometers, Detect. Assoc. Equip. **491**(1-2), 291–301 (2002).

40. F. Riva, "Development of new thin film scintillators for high-resolution x-ray imaging," Ph.D. thesis (2016).

41. M. Nikl and A. Yoshikawa, "Recent r&d trends in inorganic single-crystal scintillator materials for radiation detection," Adv. Opt. Mater. **3**(4), 463–481 (2015).

42. C. Grünzweig, G. Frei, E. Lehmann, G. Kühne, and C. David, "Highly absorbing gadolinium test device to characterize the performance of neutron imaging detector systems," Rev. Sci. Instrum. **78**(5), 053708 (2007).

43. G. D. Boreman, *Modulation transfer function in optical and electro-optical systems*, vol. 4 (SPIE press Bellingham, WA, 2001).

44. H. Fujita, D.-Y. Tsai, T. Itoh, K. Doi, J. Morishita, K. Ueda, and A. Ohtsuka, "A simple method for determining the modulation transfer function in digital radiography," IEEE Trans. Med. Imaging **11**(1), 34–39 (1992).

45. K. Tobin, P. Bingham, and J. Gregor, "Mathematics of neutron imaging," in *Neutron imaging and applications*, (Springer, 2009), pp. 109–127.

46. U. Bonse and F. Busch, "X-ray computed microtomography (uct) using synchrotron radiation (sr)," Prog. Biophys. Mol. Biol. **65**(1-2), 133–169 (1996).

47. J. Vila-Comamala, Y. Pan, J. Lombardo, W. M. Harris, W. Chiu, C. David, and Y. Wang, "Zone-doubled fresnel zone plates for high-resolution hard x-ray full-field transmission microscopy," J. Synchrotron Radiat. **19**(5), 705–709 (2012).

48. R. P. Nieuwenhuizen, K. A. Lidke, M. Bates, D. L. Puig, D. Grünwald, S. Stallinga, and B. Rieger, "Measuring image resolution in optical nanoscopy," Nat. Methods **10**(6), 557–562 (2013).

49. M. Van Heel and M. Schatz, "Fourier shell correlation threshold criteria," J. Struct. Biol. **151**(3), 250–262 (2005).

50. J. Jörissen, T. Turek, and R. Weber, "Chlorherstellung mit sauerstoffverzehrkathoden. energieeinsparung bei der elektrolyse," Chem. unserer Zeit **45**(3), 172–183 (2011).

51. I. Moussallem, J. Jörissen, U. Kunz, S. Pinnow, and T. Turek, "Chlor-alkali electrolysis with oxygen depolarized cathodes: history, present status and future prospects," J. Appl. Electrochem. **38**(9), 1177–1194 (2008).

52. D. Franzen, B. Ellendorff, M. C. Paulisch, A. Hilger, M. Osenberg, I. Manke, and T. Turek, "Influence of binder content in silver-based gas diffusion electrodes on pore system and electrochemical performance," J. Appl. Electrochem. **49**(7), 705–713 (2019).

53. M. Gebhard, M. Paulisch, A. Hilger, D. Franzen, B. Ellendorff, T. Turek, I. Manke, and C. Roth, "Design of an in-operando cell for x-ray and neutron imaging of oxygen-depolarized cathodes in chlor-alkali electrolysis," Materials **12**(8), 1275 (2019).

54. M. C. Paulisch, M. Gebhard, D. Franzen, A. Hilger, M. Osenberg, N. Kardjilov, B. Ellendorff, T. Turek, C. Roth, and I. Manke, "Operando laboratory x-ray imaging of silver-based gas diffusion electrodes during oxygen reduction reaction in highly alkaline media," Materials **12**(17), 2686 (2019).

55. L. I. Rudin, S. Osher, and E. Fatemi, "Nonlinear total variation based noise removal algorithms," Phys. D **60**(1-4), 259–268 (1992).

56. P. Coupé, P. Yger, S. Prima, P. Hellier, C. Kervrann, and C. Barillot, "An optimized blockwise nonlocal means denoising filter for 3-d magnetic resonance images," IEEE Trans. Med. Imaging **27**(4), 425–441 (2008).

57. P.-A. Douissard, A. Cecilia, X. Rochet, X. Chapel, T. Martin, T. van de Kamp, L. Helfen, T. Baumbach, L. Luquot, X. Xiao, J. Meinhardt, and A. Rack, "A versatile indirect detector design for hard x-ray microimaging," J. Instrum. **7**(09), P09016 (2012).